**ORIGINAL PAPER**

# Diffusion-Driven Frictional Aging in Silicon Carbide

Even Marius Nordhagen[1] · Henrik Andersen Sveinsson[1] · Anders Malthe-Sørenssen[1]

## Abstract
Friction is the force resisting relative motion of objects. The force depends on material properties, loading conditions and external factors such as temperature and humidity, but also contact aging has been identified as a primary factor. Several aging mechanisms have been proposed, including increased "contact quantity" due to plastic or elastic creep and enhanced "contact quality" due to formation of strong interfacial bonds. However, comparatively less attention has been given to other mechanisms that enhance the "contact quantity". In this study, we explore the influence of crystal faceting on the augmentation of "contact quantity" in cubic silicon carbide, driven by the minimization of surface free energy. Our observations reveal that the temporal evolution of the frictional aging effect follows a logarithmic pattern, akin to several other aging mechanisms. However, this particular mechanism is driven by internal capillary forces instead of the normal force typically associated with friction. Due to this fundamental distinction, existing frictional aging models fail to comprehensively explain the observed behavior. In light of these findings, we derive a model for the evolution of contact area caused by diffusion-driven frictional aging, drawing upon principles from statistical mechanics. Upon application of a normal force, the friction force is increased due to plastic creep. This investigation presents an alternative explanation for the logarithmic aging behavior observed and offers the potential to contribute to the development of more accurate friction models.

**Graphical Abstract**
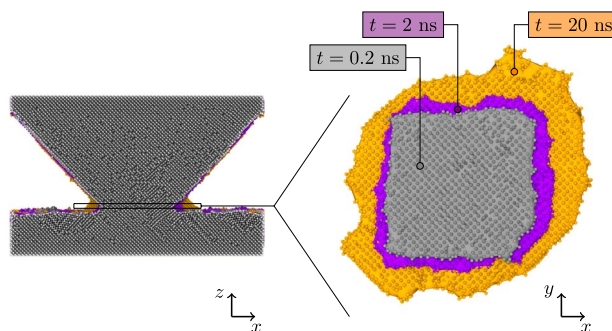


**Keywords** Frictional aging · Nanotribology · Surface diffusion · Molecular dynamics · Faceting

✉ Even Marius Nordhagen
evenmn@mn.uio.no

Henrik Andersen Sveinsson
h.a.sveinsson@fys.uio.no

Anders Malthe-Sørenssen
malthe@fys.uio.no

1    The Njord Center and Department of Physics, University of Oslo, Sem Sælands vei 24, 0316 Oslo, Norway

## 1 Introduction

Frictional aging is a phenomenon in which the strength of the interface between two contacting surfaces changes over time under static loading conditions. This idea was first suggested by Ernst Rabinowich in a pioneering study from 1951, in which he proposed that frictional aging is responsible for the dissimilarity between static and dynamic friction [1]. Additionally, it has been proposed that frictional aging

is responsible for the velocity-weakening effect observed in dynamic friction [2], thus frictional aging is of fundamental importance in friction science [3]. A deeper understanding of frictional aging is important as it affects the behavior of many mechanical systems, such as brakes, clutches and bearings. Furthermore, frictional aging plays a role in many natural phenomena, such as earthquakes [4], landslides [5] and glacier flow [6], so studying it can lead to a better understanding of these events and how to mitigate their impacts.

Two possible mechanisms of processes causing frictional aging have been proposed [7]. One is the increase in the actual area of adhesive contacts between surfaces, also known as "contact quantity". The other mechanism involves an increase in the strength of these contacts, referred to as "contact quality". Both of these mechanisms have been observed in experiments and are believed to play a significant role in frictional aging. A study by Dieterich and Kilgore demonstrated how the contact area increases with contact age due to creep [8], while Li et al. showed that strong interfacial bonds can form without a corresponding increase in contact area [9]. Simultaneous occurrence of the two mechanisms is also plausible [10]. A recent study suggests a notable amplification of contact aging under the influence of shear stress [11]. The time-dependent nature of both increased contact quantity and enhanced contact quality, both of which exhibit a logarithmic behavior, can make it challenging to ascertain which mechanism is operating in a particular case. Presently, the employed friction models are of empirical nature, requiring the derivation of their parameters through experimental investigations rather than relying on inherent material constants [12]. Consequently, this limitation prevents us from predicting friction behavior without conducting experimental studies.

Atomistic simulations have been proposed as a promising method to bridge the gap between microscale friction behavior and macroscale laws, to enhance our understanding of frictional aging [13–15]. Atomistic simulations can offer valuable information that may be difficult to acquire through real-world experiments. Specifically, since the positions, velocities, and forces of all particles are known at each time step, the spatial and temporal resolution is only restricted by the length of a time step. Molecular dynamics simulations have already demonstrated their capability as friction simulators [16–20], and have provided insights that are currently unattainable in the laboratory with the available technology.

To investigate frictional aging at the microscopic level, we model a silicon carbide asperity on a silicon carbide substrate. When the asperity and the substrate are brought in contact, the contact area grows with time due to diffusion, in a recrystallization process driven by surface energy minimization. Such recrystallization is typically a slow process that necessitates longer time scales than are available in atomistic simulations. For example, quartz crystals develop naturally over many years under high pressure and temperature, while diamond formation may take hundreds of millions of years [21]. However, silicon carbide has high surface diffusion at temperatures well below the melting point [22, 23], allowing for diffusion-limited processes to be studied within the time scales accessible in molecular dynamics simulations [24]. This feature enables atomistic simulations of processes that are impractical for most other materials. Molecular simulations of silicon carbide systems can therefore be considered model systems for general aspects of aging.

Friction experiments of silicon carbide have been conducted both in the laboratory [25, 26] and through computer simulations [27], and they are often motivated by industrial applications [28]. To our knowledge, experiments have not yet been conducted in temperature regimes where recrystallization resulting from surface diffusion is significant. In this study, we investigate the frictional aging of silicon carbide interfaces using molecular dynamics simulations at temperatures where surface diffusion is substantial, to determine how the frictional strength of a silicon carbide asperity contact evolves with aging time at various temperature. From this time evolution, we suggest a simple energy activation based model for the growth of the contact area and the friction force.

## 2 Simulations

We perform molecular dynamics simulations to study aging and frictional properties of a silicon carbide nano-asperity on a silicon carbide substrate, as illustrated in Fig. 1. The nano-asperity is prepared by carving out a rectangular octahedron from a cubic silicon carbide (3C–SiC) crystal with distance 11.19 nm between the (110) planes and the center of the asperity. Then, a rhombic dodecahedron with distance 11.70 nm between the (111) planes and the center of the asperity is carved out making the asperity shape close to the Wulff shape of our model silicon carbide [24]. The asperity is attached to a rigid top plate that is used to impose a normal load and lateral motion on the asperity. The normal load is imposed by adding a force to the top plate particles, and the lateral motion is imposed by controlling the lateral position of the top plate. The bottom 1 nm of the substrate is rigid and fixed in all directions to keep the substrate in place, and the 1 nm above the fixed layer is kept at a constant temperature using a Langevin thermostat. The uppermost 1 nm of the asperity (just under the top plate) is also kept at constant temperature using a Langevin thermostat. The non-rigid parts are integrated using Newton's 2nd law, to avoid disturbing the dynamics in the process region. This is the *de facto* standard setup of atomistic friction simulations, and has been used in many recent studies [13, 20, 29]. The

**Fig. 1** Illustration of the system immediately after the asperity and the substrate are brought in contact. During the simulations the lower part of the substrate and the plate that the asperity is attached to are held rigid (orange layers). The upper part of the asperity and the layer above the rigid layer of the substrate are controlled by a thermostat (blue layers). System dimensions are marked with double-headed arrows (Color figure online)
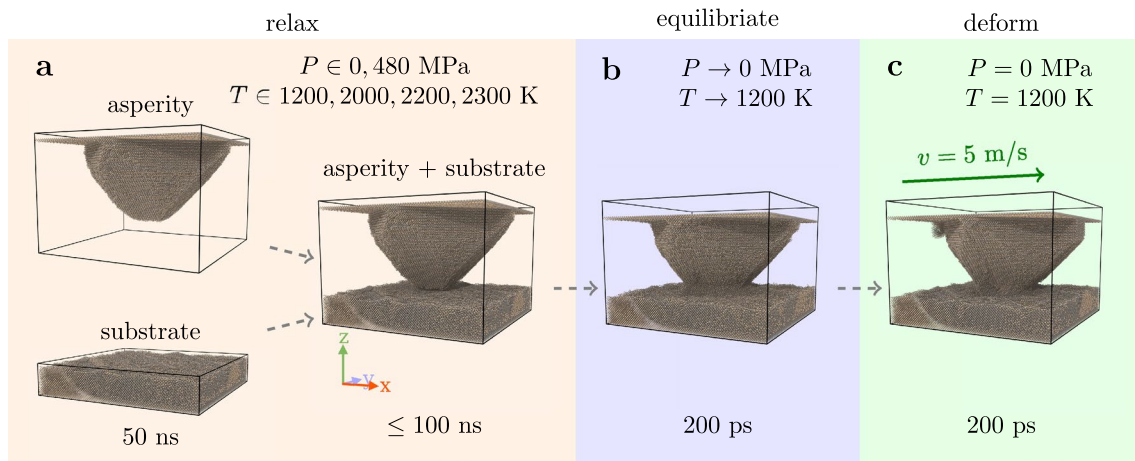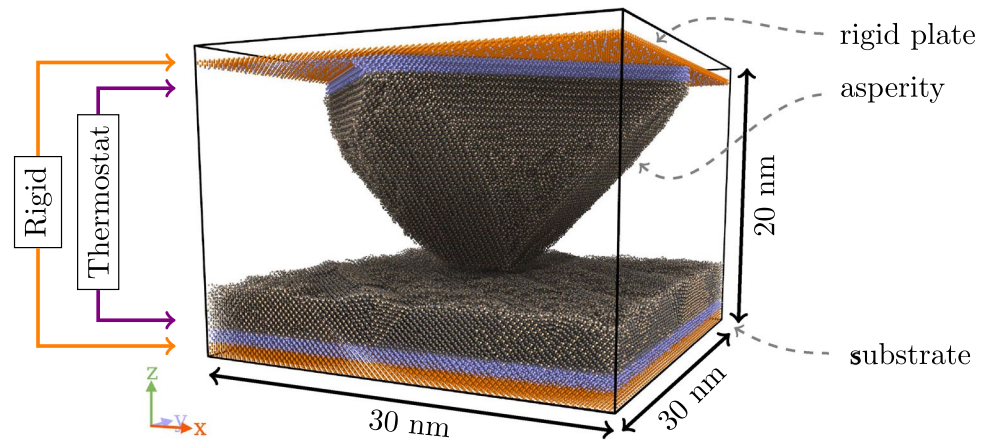


**Fig. 2** An illustration of the three simulation steps. In **a** an asperity and a substrate are relaxed separately for 50 ns, at a temperature $T$. Thereafter, they are brought in contact and relaxed for up to 100 ns under a pressure $P$. In **b** the system is equilibriated by gradually reducing the pressure to zero and the temperature to 1200 K, for 200 ps. In **c** the system is deformed by applying a constant velocity on the upper part of the asperity for 200 ps

overall system size is $30 \times 30 \times 20$ nm, with 866,918 atoms, half of them silicon and half of them carbon.

To assess the aging effect on static friction of the silicon carbide nano-asperity, we perform molecular dynamics simulations in three steps: relaxation, equilibration and deformation (see Fig. 2).

## 2.1 Relaxation

First, we relax an asperity and a substrate in separate simulation cells for 50 ns at a temperature in the range [2000, 2300] K.[1] This first step is taken to bring the substrate and asperity close to equilibrium configurations so that particle fluxes observed in aging simulations are due to aging of the

asperity-substrate contact. During this first step the asperity relaxes to its Wulff shape, and the substrate becomes rough. Figure 3 displays substrates relaxed for 50 ns at some selected temperatures and is discussed below.

Thereafter, the asperity and substrate are placed into the same simulation box, separated by a distance of 4 Å, and relaxed. During this relaxation, the asperity gets pulled towards the substrate due to a cohesive force originating from induced charge-dipole and dipole-dipole interactions. The substrate and the asperity are therefore spontaneously brought into contact.

## 2.2 Equilibration

We then let the system evolve through time at a temperature in the range [2000, 2300] K and pressure in 0, 480 MPa and monitor the contact area (Fig. 2a). The simulation is run for 20 ns (except from a simulation at $T = 2300$ K, $P = 0$ MPa

---

[1] For the case with an applied normal force, we run an additional simulation at low temperature ($T = 1200$ K).
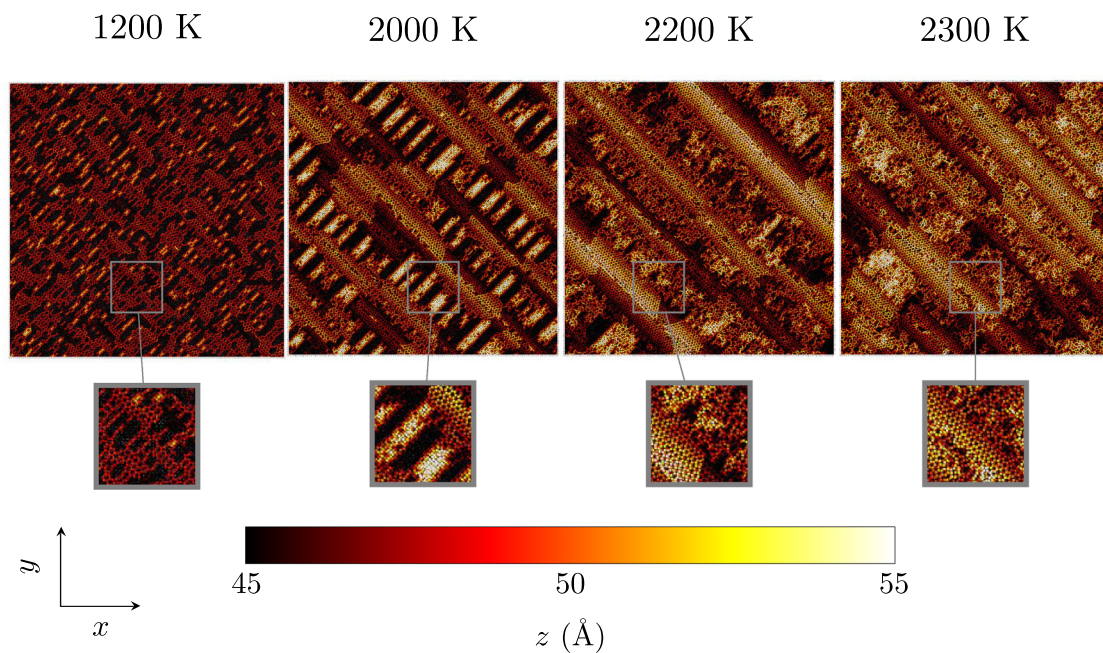
**Fig. 3** The figure shows the top view of the substrates following a 50 ns relaxation period at various temperatures. Magnified windows are included to highlight interesting regions of the substrates. The atoms are colored based on their $z$-position, where brighter colors indicate larger $z$-components (Color figure online)

that was run for 70 ns), and during this time the contact area grows. We refer to the simulation time in this phase as the *contact age*. We extract system configurations at different contact ages. These systems are equilibrated by gradually decreasing the temperature to 1200 K, and the pressure to 0 MPa over a time period of 200 ps (Fig. 2b).

## 2.3 Deformation

Lastly, the static friction of the system is assessed by translating the rigid layer of the asperity at a constant velocity of 5 m/s in the $x$-direction and measuring the shear force by which the system resists this translation (Fig. 2c).

## 2.4 Equilibrating the Substrate

The initial relaxation of the substrate results in a rough surface with nano-ribbons, as shown in Fig. 3. Major nano-ribbons (ribbons traversing boundary to boundary) are present at all temperatures we have examined. These ribbons are formed because the (110) planes have lower energies than the (100) surfaces [24]. At temperatures around 2000 K, we also observe additional small ribbons between the major ribbons. Corresponding equilibrium shapes of the asperity for the various temperatures can be found in the supplementary material.

## 2.5 Computational Details

Molecular dynamics simulations of the nano-asperity system are performed using LAMMPS [30], with the silicon carbide force field and parameters proposed by Vashishta et al. [31]. To integrate the rigid body, a symplectic integrator [32] is used and atoms in contact with the rigid body are controlled using a Nosé-Hoover thermostat [33, 34]. For atoms in the mobile region ($z \in [2, 18.6]$ nm), the Verlet integration scheme [35] is used with a time step of 1 fs for simulations with normal pressure and 2 fs for simulations without normal pressure. A Langevin thermostat [36] is applied to the regions defined by $z \in [1, 2]$ nm and $[18.6, 19.6]$ nm with a damping time of 1.0 ps to set the temperature of the system. Periodic boundary conditions are applied in the horizontal directions, while fixed boundaries are used in the $z$-direction. All simulations are carried out on NVIDIA A100 graphics cards using the KOKKOS package [37] in LAMMPS. Simulating the system for 1 ns takes approximately 8 h of wall clock time with a timestep of 2 fs. The contact area, coordination analysis, and system visualization are performed using OVITO [38]. The presented results have been obtained using about 5000 GPU hours.

The initial peak in the lateral force curve, as shown in Fig. 4b (inset), is used to measure the static friction force. The lateral force represents the net force acting on the upper rigid plate in the direction of its motion. Since the total force on the asperity becomes negative when it is moved in the
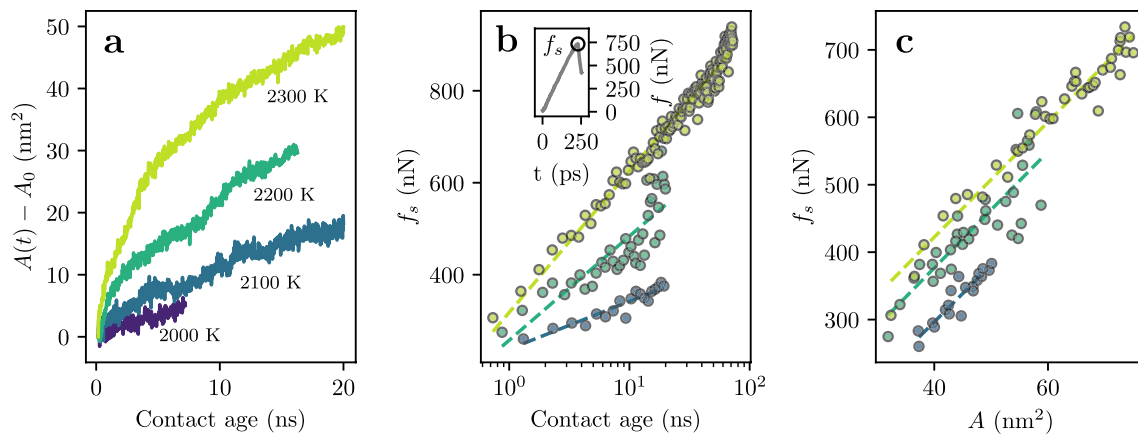
**Fig. 4** Contact area growth and static friction of silicon carbide nano-asperities aged without a normal load. **a** The increase in real contact area as a function of contact age. **b** The static friction force as a function of contact age. The inset shows an example of a loading curve, i.e. friction force as a function of time during shearing. The static friction force is measured as the maximum of the loading curve. **c** The static friction force as a function of contact area. In **a** the different graphs are labeled according to temperature, and these same colors are subsequently utilized in both (**b**) and (**c**) (Color figure online)

positive direction, we reverse the sign of the lateral force to obtain the magnitude of the static friction force, which is of primary interest.

### 2.5.1 Contact Area Measurement

The estimation of the contact area is achieved by enveloping a surface mesh around a thin slice of the asperity located in close proximity to the surface. This slice is determined using a combination of cluster and coordination analysis carried out in OVITO [38]. In this context, the term "contact area" refers to the actual contact area as described by Mo et al. [18]. More information about the procedure for measuring the contact area can be found in the supplementary material.

### 2.5.2 Rayleigh Wave Speed Measurement

The speed of Rayleigh waves in 3C–SiC crystal was determined by performing a series of deformation simulations, as explained in Refs. [39, 40]. The simulations were carried out for various temperatures $T \in \{1, 1800, 2000, 2200, 2300\}$, using a 3C–SiC crystal with dimensions of $10 \times 10 \times 10$ nm. To reach equilibrium, the crystal was initially relaxed in the isobaric-isothermal ensemble at $P = 1$ bar for 20 ps, and the average cell dimensions of the simulation box were sampled. The simulation box was then gradually resized to that average box size. Finally, the crystal was relaxed in the isothermal ensemble for another 20 ps.

To estimate the elastic constants $c_{11}$, $c_{13}$, $c_{33}$, and $c_{55}$, separate simulations were performed in which the crystal was compressed 0.1 nm in the $x$- and $z$-directions to determine the normal stresses $\sigma_{xx}$ and $\sigma_{zz}$, respectively. The remaining elastic constant, $c_{55}$, was estimated by conducting a shear deformation simulation in the $xz$-direction to obtain the shear stress component $\sigma_{xz}$.

## 3 Results and Discussions

The main outputs that we collect from simulations are the evolution of the contact area and the maximum static friction force through time. Figure 4 shows the contact area evolution through time (4a), the friction force as a function of contact age (4b) and the friction force as a function of the contact area (4c) for the system where only cohesion brings the asperity in contact with the substrate. In Sect. 3.1, we develop a candidate model to explain the contact area evolution quantitatively. Model fits are plotted on top of area evolution data in Fig. 5. We discuss the friction force, the contact area and the relationship between them in Sect. 3.2, and the effect of aging under a normal load in Sect. 3.3. Figure 6 shows the contact area and static friction force data for the system that is aged under a 480 MPa normal load. In Sect. 3.4, we analyze the detailed failure mechanism when the static friction force is overcome. This failure mechanism is illustrated in Fig. 7.

### 3.1 Contact Area Evolution

In Fig. 4, a monotonic and seemingly logarithmic growth of the contact area with time can be observed across all temperatures. The rate of area growth is directly influenced by the temperature, with higher temperatures resulting in faster growth. This phenomenon arises due to the formation of facets around the asperity in our two-crystal system, comprising an equilibrated asperity and substrate.
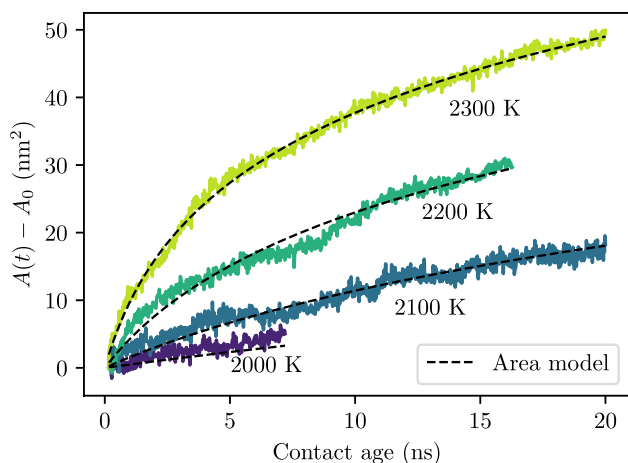
**Fig. 5** Model fits of the model in Eq. 5 plotted on top of the raw contact area data as a function of time. The various graphs are labeled by temperature

The combination of these crystals creates a nonequilibrium system characterized by a high surface free energy in the junction formed between the substrate and the asperity (referred to as the *notch region*). The growth of the contact area in our system is driven by internal capillary forces that induce facet formation within the notch region. During facet formation, the crystal lattices remain perfectly aligned, suggesting a constant crystal density. Consequently, this process can be effectively modeled by considering volume-conserved shape changes. Building upon our observations, we propose a model to explain the evolution of the contact area based on the theory of volume-conserving shape changes in nonequilibrium crystals, as previously described by Rohrer et al. [41]. Facets are

formed through layer-by-layer growth, and the nucleation energy barrier for each layer depends on the free energy associated with a nucleus covering half of the facet area. We denote the nucleation energy barrier for adding and removing facet layers as $E_b^+$ and $E_b^-$, respectively. The net nucleation rate is then expressed as

$$I = f_+ \exp\left(-\frac{E_b^+}{k_B T}\right) - f_- \exp\left(-\frac{E_b^-}{k_B T}\right),\tag{1}$$

where $k_B$ is the Boltzmann constant and $f_+$ and $f_-$ are attempt frequencies. Since facet formation in the notch region is energetically favored, we neglect the removal of facet layers in our model. We assume that facet formation is proportional to the nucleation rate, and that the nucleation energy barrier is a function of the number of layers formed, $n$, such that $E_b(n) \equiv E_b^+$ and $f \equiv f_+$. The differential equation to be solved is thus given by

$$\frac{\mathrm{d}n}{\mathrm{d}t} = f \exp\left(-\frac{E_b(n)}{k_B T}\right).\tag{2}$$

The solution of this equation depends heavily on the choice of nucleation energy barrier. Rohrer et al. found that the nucleation energy barrier for the growth of facet layers is directly proportional to the corresponding facet area [41]. In our system, as facet layers are added, the facet area progressively expands, primarily in the direction that is normal both to the layer growth direction and to the contact perimeter (see Fig. 6 in supplementary materials). Consequently, we propose an activation energy expression of the form $E_b(n) = E_b(0) + an$, where $E_b(0)$ denotes the initial energy barrier, and $a > 0$ signifies the rate of energy barrier
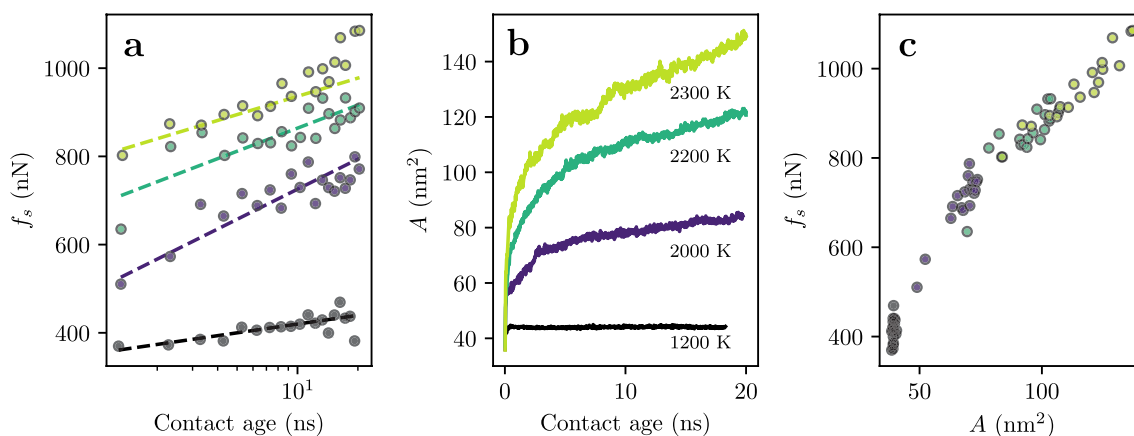


**Fig. 6** Contact area growth and static friction of silicon carbide nano-asperities aged under a normal load of $P = 480$ MPa. **a** The static friction force as a function of contact age. **b** Real contact area as a function of contact age. **c** The static friction force as a function of

contact area. In **b** the different graphs are labeled according to temperature, and these same colors are subsequently utilized in both (**a**) and (**c**) (Color figure online)
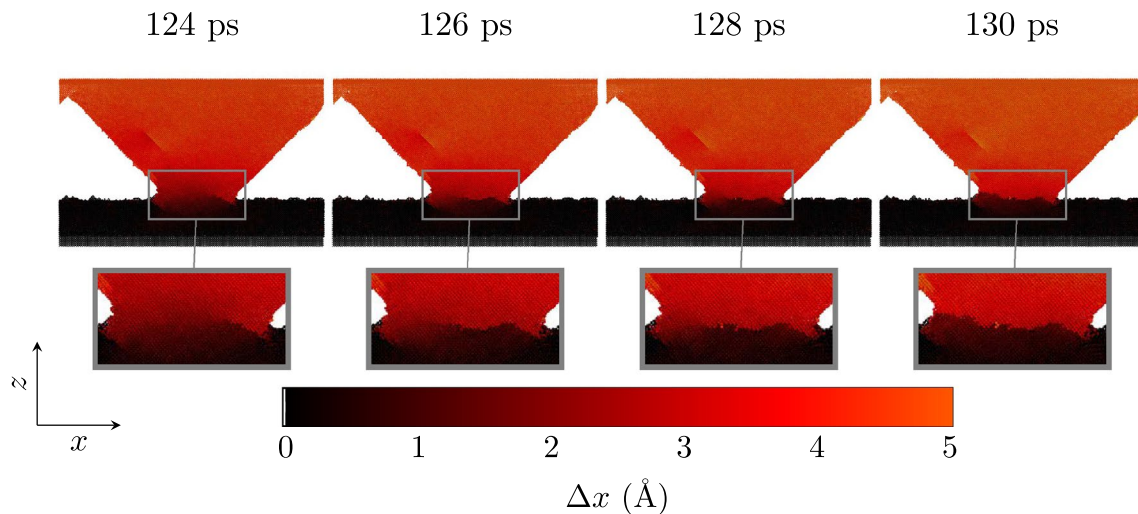
**Fig. 7** Cross section view of an asperity undergoing rupture for four different times given relative to the start of deformation. Atoms colors indicate their displacement in *x*-direction ($\Delta x$) since the onset of deformation. The rupture area is magnified and displayed in sepa-rate windows. The simulation was performed at a temperature of $T = 2000$ K, normal pressure of $P = 480$ MPa, and the system was relaxed for 18 ns before deformation (Color figure online)

increase. For a more detailed derivation, please refer to the "Contact area model" in the supplementary material. The differential equation then simplifies to

$$\frac{dn}{dt} = f \exp\left(-\frac{E_b(0)}{k_B T}\right) \exp\left(-\frac{an}{k_B T}\right). \quad (3)$$

Assuming that the number of facet layers is the only quantity that evolves with time, the analytical solution to this equation is given by

$$n(t) = \frac{k_B T}{a} \log\left(1 + \frac{at}{k_B T} f \exp\left(-\frac{E_b(0)}{k_B T}\right)\right). \quad (4)$$

The mathematical form of this model resembles the aging law by Dieterich [42], and a similar derivation can be performed for frictional aging due to creep [43, 44].

To establish the relationship between the contact area and the number of facet layers, certain assumptions need to be made regarding the shape of the contact interface. Given that the initial contact interface is approximately square-shaped, one possibility is that it remains square-shaped throughout the aging simulation. Consequently, the relationship between the contact area and the number of facet layers can be described by $A(n) = A(0) + 4\sqrt{2}snd + 8(nd)^2$, with $A(0) = s^2$ as the initial contact area, *s* as the initial width of the contact and *d* as the thickness of a facet layer. In the case of a circular contact interface, the contact area evolution can be described as $A(n) = A(0) + \sqrt{2}\pi snd + 2\pi(nd)^2)$ with $A(0) = s^2\pi/4$. The inclusion of the factor $\sqrt{2}$ arises from the 45° angle at which the facets form with the substrate,

resulting in a facet layer width of $\sqrt{2}d$ as observed from the substrate. Although the true contact shape likely lies between square and circular based on observations, assuming $s \gg nd$, we can approximate $A(n)$ as $A(0) + cn$ in both cases. This approximation leads to the contact area model:

$$A(t) = A(0) + c\frac{k_B T}{a} \log\left(1 + \frac{at}{k_B T} f \exp\left(-\frac{E_b(0)}{k_B T}\right)\right), \quad (5)$$

where *c* represents the proportionality constant between the contact area and the number of facet layers. This model incorporates the material-dependent parameters *a*, *f*, and $E_b(0)$, and a singularity as $t \to 0$, which is extensively discussed in the literature [2, 45, 46], is avoided. For a more detailed and comprehensive derivation of the contact area model, please refer to the supplementary materials.

Figure 5 illustrates the fitting of the contact evolution model, described by Eq. 5, to the contact area evolution graphs at different temperatures. The proportionality constant between contact area and number of facet layers were determined to be $c = 4\sqrt{2}sd \approx 9.5$ nm$^2$, with $s = 54$ Å and $d = 3.1$ Å. The optimized parameters for the fitting process were determined as $f = 3.2 \times 10^9 ns^{-1}$, $E_b(0) = 4.3$ eV, and $a = 0.1088$ eV. A change in *c* can be accounted for by *a* and *f*. Upon visual inspection, the fit appears to be satisfactory, and this observation is supported by a root-mean squared error of 1.104 nm$^2$ and an $R^2$-score of 0.9937. These metrics provide quantitative confirmation of the fitting quality. Notably, it is worth highlighting that the fitting parameters closely correspond to fundamental material constants.

**Table 1** Rayleigh wave speed and elastic constants for 3C–SiC at various temperatures

| $T$ (K) | $\rho$ (kg/m³) | $c_{11}$ (GPa) | $c_{13}$ (GPa) | $c_{33}$ (GPa) | $c_{55}$ (GPa) | $c_R$ (m/s) |
|---|---|---|---|---|---|---|
| 1 | 3217 | 396.45 | 150.58 | 396.38 | 68.18 | 4494 |
| 1800 | 3038 | 286.22 | 107.68 | 297.10 | 51.83 | 4027 |
| 2000 | 3016 | 266.80 | 97.32 | 286.35 | 49.99 | 3968 |
| 2200 | 2986 | 239.72 | 70.07 | 240.47 | 46.84 | 3855 |

Here, $\rho$ is the crystal density, $c_{ij}$ are the elastic constants as defined in Ref. [40] and $c_R$ is the Rayleigh wave speed

## 3.2 Friction Force and Contact Area

The static friction behavior, as illustrated in Fig. 4b, predominantly demonstrates a logarithmic increase over time across all the temperatures examined. However, for temperatures 2200 K and 2300 K, there is a hint of positive curvature emerging after long simulation durations, indicating a frictional aging behavior that surpasses the logarithmic trend. Notably, a recent study observed a linear aging behavior in silica-silica contacts within the timescales of approximately 5 to 90 ms, attributed to interfacial reaction kinetics [47]. Exploring this frictional regime further would necessitate microsecond-scale simulations, which are challenging to accomplish within our current system constraints. The rate of this logarithmic increase is primarily influenced by the contact area and demonstrates a positive correlation with temperature. The static friction value represents the maximum frictional force that the system can sustain, as indicated in the inset of Fig. 4. Figure 4c illustrates the relationship between static friction and contact area. It reveals a strong correlation, suggesting that the friction force is approximately proportional to the contact area. Although there may be slight curvature in the data points, particularly at $T = 2300$ K, it remains uncertain whether this observation is coincidental or a genuine effect due to the limited range of contact areas analyzed. Furthermore, the data indicates that, for a given contact area, contact strengths are arranged in a manner that implies stronger contacts at higher temperatures. Considering that all the deformation simulations were conducted at the same temperature (1200 K), this is a nontrivial behavior that suggests that the temperature history is important for the friction-area proportionality. One potential explanation could be a decrease in bond density at higher temperatures, although this hypothesis calls for additional exploration.

## 3.3 Effect of a Normal Load

In Fig. 6a, we demonstrate that applying a normal load exhibiting a pressure of $P = 480$ MPa significantly increases the initial static friction force for all temperatures. However, this does not amplify the aging effect that leads to an increase in frictional strength over time. Surprisingly, the aging effect appears to be slightly weaker with the application of the normal pressure. For example, at temperature $T = 2300$ K the change in static friction force during the first 20 nanoseconds is about $\Delta f_s \approx 300$ nN with a normal pressure of $P = 480$ MPa, as compared to $\Delta f_s \approx 400$ nN without any normal pressure (as previously shown in Fig. 4a). Despite the decreased aging effect, the contact area seems to increase more quickly than without a normal force (as seen in Fig. 6b). Consequently, the static friction force is not completely proportional to the contact area. At larger contact areas, the force per area is smaller than at smaller contact areas (as depicted in Fig. 6c). This non-proportional relationship between friction and area has been observed in several other studies, such as in Refs. [8, 48–50]. Kilgore et al. suggest that any newly formed contact area lacks shear strength [48], causing the contact area to grow faster than the friction force. More investigations is needed to understand whether or not this is the mechanism at work here.

## 3.4 Mechanical Failure Mechanism

Figure 7 illustrates the shear displacement of particles in a crystalline system at 2000 K in the direction of movement as the asperity slips. Notably, cracks emerge in areas characterized by a significant gradient of shear displacement. These regions can be identified in Fig. 7 by a sharp color change. The zoomed-in inset depicts that the rupture propagates from the leading edge (end of asperity on the right-hand side) to the trailing notch (the notch on the left-hand side), which is a commonly observed rupture front. However, there is no particular tendency in terms of which direction the crack propagates. Vertical cracks on the left side of the asperity is another usual observation, like shown in the supplementary material.

From Fig. 7, the rupture velocity can be estimated to be about 1300 m/s, given that the contact's diameter is approximately 8 nm. We employed the procedure presented in Refs. [39, 40] to determine the Rayleigh wave speed in 3C–SiC and determine whether this rupture can be considered rapid. For a comparable temperature, the Rayleigh wave speed in the modelled silicon carbide crystal was calculated to be 3968 m/s, which is roughly three times faster than the rupture. Thus, the observed ruptures are relatively rapid. Table 1

provides the Rayleigh wave speed of crystalline 3C–SiC at other relevant temperatures, along with the crystal density and elastic constants utilized to estimate the speed. These constants can also be used to determine material properties like the bulk, shear and Young's modulus, as well as the Poisson ratio. The elastic constants are consistent with the ones found in [51], and the measured Rayleigh wave speeds agree with theoretical [52] and experimental [53] values.

## 4 Conclusions and Perspectives

We have used molecular dynamics simulations to investigate frictional aging in a silicon carbide system. We have found that the static friction force increases logarithmically with contact age even without an externally applied normal load on the asperity. The growth in the static friction force is attributed to the growth of the real contact area due to facet formation in silicon carbide.

A candidate model for the evolution of contact area was formulated utilizing principles from nucleation theory. This model estimates a logarithmic growth in contact area as a function of time, mirroring the observed behaviors in frictional aging attributed to creep and the formation of stronger interfacial bonds. These mechanisms can be described by thermally activated processes, suggesting a universal logarithmic behavior in frictional aging resulting from thermally activated bond formation with an increasing energy barrier.

In the presence of a normal load, the initial static friction is observed to be higher compared to the case without a normal load. However, the rate of increase in static friction over time does not exhibit a significant difference when a normal load is applied compared to when no normal load is present. Moreover, there is a clear non-linearity between static friction and contact area in this case, which may be explained by a non-uniform stress concentration across the contact interface. For the failure mechanism, we found semi-rapid ruptures of approximately one third of the Rayleigh wave speed, either propagating from the leading edge to the trailing notch or in the opposite direction.

Future investigations could focus on exploring the non-linear relationship between friction and contact area, with particular attention to studying interfacial stress concentration in greater detail. Silicon carbide's unique properties make it an intriguing material for studying various tribological and tribochemical phenomena. Subsequent studies could involve sliding simulations to investigate dynamic friction, wear, and sliding history effects on friction.

Further research could also explore diffusion-driven frictional aging with different silicon carbide asperity shapes to (i) assess the influence of the asperity shape on the frictional behavior and (ii) verify that the modeling approach we take in Sect. 3.1 works for other contact geometries as well.

However, only asperity shapes that are stable, or at least metastable can be used, since otherwise they will readily deform into their equilibrium shape at temperatures where surface diffusion is significant.

## Declarations

## References

1. Rabinowicz, E.: The nature of the static and kinetic coefficients of friction. J. Appl. Phys. **22**(11), 1373–1379 (1951). https://doi.org/10.1063/1.1699869
2. Dieterich, J.H.: Time-dependent friction and the mechanics of stick-slip. In: Byerlee, J.D., Wyss, M. (eds.) Rock friction and earthquake prediction. Contributions to current research in geophysics (CCRG), pp. 790–806. Birkhäuser, Basel (1978). https://doi.org/10.1007/978-3-0348-7182-2_15
3. Krylov, S.Y., Frenken, J.W.M.: The physics of atomic-scale friction: Basic considerations and open questions. Phys. Status Solidi (b) **251**(4), 711–736 (2014). https://doi.org/10.1002/pssb.201350154
4. Scholz, C.H.: The mechanics of earthquakes and faulting, 3rd edn. Cambridge University Press, Cambridge (2019). https://doi.org/10.1017/9781316681473
5. Handwerger, A.L., Rempel, A.W., Skarbek, R.M., Roering, J.J., Hilley, G.E.: Rate-weakening friction characterizes both slow sliding and catastrophic failure of landslides. Proc. Natl. Acad. Sci. **113**(37), 10281–10286 (2016). https://doi.org/10.1073/pnas.1607009113

6. Lipovsky, B.P., Dunham, E.M.: Slow-slip events on the Whillans ice plain, Antarctica, described using rate-and-state friction as an ice stream sliding law. J. Geophys. Res.: Earth Surf. **122**(4), 973–1003 (2017). https://doi.org/10.1002/2016JF004183

7. Dieterich, J.H.: Time-dependent friction in rocks. J. Geophys. Res. (1896–1977) **77**(20), 3690–3697 (1972). https://doi.org/10.1029/JB077i020p03690

8. Dieterich, J.H., Kilgore, B.D.: Direct observation of frictional contacts: new insights for state-dependent properties. Pure Appl. Geophys. **143**(1), 283–302 (1994). https://doi.org/10.1007/BF00874332

9. Li, Q., Tullis, T.E., Goldsby, D., Carpick, R.W.: Frictional ageing from interfacial bonding and the origins of rate and state friction. Nature **480**(7376), 233–236 (2011). https://doi.org/10.1038/nature10589

10. Li, Z., Szlufarska, I.: Chemical creep and its effect on contact aging. ACS Mater. Lett. **4**(7), 1368–1373 (2022). https://doi.org/10.1021/acsmaterialslett.2c00356

11. Vorholzer, M., Dietzel, D., Cihan, E., Schirmeisen, A.: Shear-assisted contact aging of single-asperity nanojunctions. Phys. Rev. B **105**(19), 195401 (2022). https://doi.org/10.1103/PhysRevB.105.195401

12. Marone, C.: On the rate of frictional healing and the constitutive law for time- and slip-dependent friction. Int. J. Rock Mech. Min. Sci. **34**(3), 187–118717 (1997). https://doi.org/10.1016/S1365-1609(97)00054-3

13. Dong, Y., Li, Q., Martini, A.: Molecular dynamics simulation of atomic friction: a review and guide. J. Vac. Sci. Technol. A **31**(3), 030801 (2013). https://doi.org/10.1116/1.4794357

14. Spikes, H.: Stress-augmented thermal activation: tribology feels the force. Friction **6**(1), 1–31 (2018). https://doi.org/10.1007/s40544-018-0201-2

15. ...Vakis, A.I., Yastrebov, V.A., Scheibert, J., Nicola, L., Dini, D., Minfray, C., Almqvist, A., Paggi, M., Lee, S., Limbert, G., Molinari, J.F., Anciaux, G., Aghababaei, R., Echeverri Restrepo, S., Papangelo, A., Cammarata, A., Nicolini, P., Putignano, C., Carbone, G., Stupkiewicz, S., Lengiewicz, J., Costagliola, G., Bosia, F., Guarino, R., Pugno, N.M., Müser, M.H., Ciavarella, M.: Modeling and simulation in tribology across scales: an overview. Tribol. Int. **125**, 169–199 (2018). https://doi.org/10.1016/j.triboint.2018.02.005

16. Zhang, L., Tanaka, H.: Towards a deeper understanding of wear and friction on the atomic scale-a molecular dynamics analysis. Wear **211**(1), 44–53 (1997). https://doi.org/10.1016/S0043-1648(97)00073-2

17. Zhang, L.C., Johnson, K.L., Cheong, W.C.D.: A molecular dynamics study of scale effects on the friction of single-asperity contacts. Tribol. Lett. **10**(1), 23–28 (2001). https://doi.org/10.1023/A:1009038715458

18. Mo, Y., Turner, K.T., Szlufarska, I.: Friction laws at the nanoscale. Nature **457**(7233), 1116–1119 (2009). https://doi.org/10.1038/nature07748

19. Liu, Y., Szlufarska, I.: Chemical origins of frictional aging. Phys. Rev. Lett. **109**(18), 186102 (2012). https://doi.org/10.1103/PhysRevLett.109.186102

20. Li, A., Liu, Y., Szlufarska, I.: Effects of interfacial bonding on friction and wear at silica/silica interfaces. Tribol. Lett. **56**(3), 481–490 (2014). https://doi.org/10.1007/s11249-014-0425-x

21. Stachel, T., Luth, R.W.: Diamond formation—where, when and how? Lithos **220–223**, 200–220 (2015). https://doi.org/10.1016/j.lithos.2015.01.028

22. Ghoshtagore, R.N., Coble, R.L.: Self-diffusion in silicon carbide. Phys. Rev. **143**(2), 623–626 (1966). https://doi.org/10.1103/PhysRev.143.623

23. Hong, J.D., Hon, M.H., Davis, R.F.: Self-diffusion in alpha and beta silicon carbide. Ceram. Int. **5**(4), 155–160 (1979). https://doi.org/10.1016/0390-5519(79)90024-3

24. Sveinsson, H.A., Hafreager, A., Kalia, R.K., Nakano, A., Vashishta, P., Malthe-Sørenssen, A.: Direct atomic simulations of facet formation and equilibrium shapes of SiC nanoparticles. Cryst. Growth Des. **20**(4), 2147–2152 (2020). https://doi.org/10.1021/ACS.CGD.9B00612

25. Xiao, H., Senda, T.: Friction and wear of silicon carbide at elevated temperatures. J. Ceram. Soc. Jpn. **105**(1225), 750–755 (1997). https://doi.org/10.2109/jcersj.105.750

26. Zhao, X., Liu, Y., Wen, Q., Wang, Y.: Frictional performance of silicon carbide under different lubrication conditions. Friction **2**(1), 58–63 (2014). https://doi.org/10.1007/s40544-014-0039-1

27. Piroozan, N., Naserifar, S., Sahimi, M.: Sliding friction between two silicon-carbide surfaces. J. Appl. Phys. **125**(12), 124301 (2019). https://doi.org/10.1063/1.5086185

28. Lafon-Placette, S., Delbé, K., Denape, J., Ferrato, M.: Tribological characterization of silicon carbide and carbon materials. J. Eur. Ceram. Soc. **35**(4), 1147–1159 (2015). https://doi.org/10.1016/j.jeurceramsoc.2014.10.038

29. Schall, J.D., Milne, Z.B., Carpick, R.W., Harrison, J.A.: Molecular dynamics examination of sliding history-dependent adhesion in Si-Si nanocontacts: connecting friction, wear, bond formation, and interfacial adhesion. Tribol. Lett. **69**(2), 52 (2021). https://doi.org/10.1007/s11249-021-01431-z

30. Plimpton, S.: Fast parallel algorithms for short-range molecular dynamics. J. Comput. Phys. **117**(1), 1–19 (1995). https://doi.org/10.1006/JCPH.1995.1039

31. Vashishta, P., Kalia, R.K., Nakano, A., Rino, J.P.: Interaction potential for silicon carbide: a molecular dynamics study of elastic constants and vibrational density of states for crystalline and amorphous silicon carbide. J. Appl. Phys. **101**(10), 103515–103515 (2007). https://doi.org/10.1063/1.2724570

32. Kamberaj, H., Low, R.J., Neal, M.P.: Time reversible and symplectic integrators for molecular dynamics simulations of rigid molecules. J. Chem. Phys. **122**(22), 224114 (2005). https://doi.org/10.1063/1.1906216

33. Nosé, S.: A unified formulation of the constant temperature molecular dynamics methods. J. Chem. Phys. **81**(1), 511–519 (1984). https://doi.org/10.1063/1.447334

34. Hoover, W.G.: Canonical dynamics: equilibrium phase-space distributions. Phys. Rev. A **31**(3), 1695–1697 (1985). https://doi.org/10.1103/PhysRevA.31.1695

35. Verlet, L.: Computer "experiments" on classical fluids. I. Thermodynamical properties of Lennard-Jones molecules. Phys. Rev. **159**(1), 98–98 (1967). https://doi.org/10.1103/PhysRev.159.98

36. Schneider, T., Stoll, E.: Molecular-dynamics study of a three-dimensional one-component model for distortive phase transitions. Phys. Rev. B **17**(3), 1302–1302 (1978). https://doi.org/10.1103/PhysRevB.17.1302

37. Trott, C.R., Lebrun-Grandié, D., Arndt, D., Ciesko, J., Dang, V., Ellingwood, N., Gayatri, R., Harvey, E., Hollman, D.S., Ibanez, D., Liber, N., Madsen, J., Miles, J., Poliakoff, D., Powell, A., Rajamanickam, S., Simberg, M., Sunderland, D., Turcksin, B., Wilke, J.: Kokkos 3: Programming model extensions for the exascale era. IEEE Trans. Parallel Distrib. Syst. **33**(4), 805–817 (2022). https://doi.org/10.1109/TPDS.2021.3097283

38. Stukowski, A.: Visualization and analysis of atomistic simulation data with OVITO-the open visualization tool. Model. Simul. Mater. Sci. Eng. **18**(1), 015012–015012 (2010). https://doi.org/10.1088/0965-0393/18/1/015012

39. Guren, M.G., Sveinsson, H.A., Malthe-Sørenssen, A., Renard, F.: Nanoscale damage production by dynamic tensile rupture in

alpha-quartz. Geophys. Res. Lett. **49**(20), 2022–100468 (2022). https://doi.org/10.1029/2022GL100468

40. Vinh, P.C., Ogden, R.W.: On the Rayleigh wave speed in orthotropic elastic solids. Meccanica **40**(2), 147–161 (2005). https://doi.org/10.1007/s11012-005-1603-6

41. Rohrer, G.S., Rohrer, C.L., Mullins, W.W.: Nucleation energy barriers for volume-conserving shape changes of crystals with non-equilibrium morphologies. J. Am. Ceram. Soc. **84**(9), 6 (2001). https://doi.org/10.1111/j.1151-2916.2001.tb00965.x

42. Dieterich, J.H.: Modeling of rock friction: 1. Experimental results and constitutive equations. J. Geophys. Res.: Solid Earth **84**, 2161–2168 (1979). https://doi.org/10.1029/JB084iB05p02161

43. Brechet, Y., Estrin, Y.: The effect of strain rate sensitivity on dynamic friction of metals. Scr. Metall. Mater. **30**(11), 1449–1454 (1994). https://doi.org/10.1016/0956-716X(94)90244-5

44. Hatano, T.: Rate and state friction law as derived from atomistic processes at asperities. (2015). https://doi.org/10.48550/arXiv.1512.05078

45. Baumberger, T., Caroli, C.: Solid friction from stick-slip down to pinning and aging. Adv. Phys. **55**(3), 279–348 (2006). https://doi.org/10.1080/00018730600732186

46. Bar-Sinai, Y., Spatschek, R., Brener, E.A., Bouchbinder, E.: On the velocity-strengthening behavior of dry friction. J. Geophys. Res.: Solid Earth **119**(3), 1738–1748 (2014). https://doi.org/10.1002/2013JB010586

47. Tian, K., Li, Z., Liu, Y., Gosvami, N.N., Goldsby, D.L., Szlufarska, I., Carpick, R.W.: Linear aging behavior at short timescales in nanoscale contacts. Phys. Rev. Lett. **124**(2), 026801 (2020). https://doi.org/10.1103/PhysRevLett.124.026801

48. Kilgore, B., Lozos, J., Beeler, N., Oglesby, D.: Laboratory observations of fault strength in response to changes in normal stress. J. Appl. Mech. (2012). https://doi.org/10.1115/1.4005883

49. Kilgore, B., Beeler, N.M., Lozos, J., Oglesby, D.: Rock friction under variable normal stress. J. Geophys. Res.: Solid Earth **122**(9), 7042–7075 (2017). https://doi.org/10.1002/2017JB014049

50. Farain, K., Bonn, D.: Predicting frictional ageing from bulk relaxation measurements. (2022). arXiv https://doi.org/10.48550/arXiv.2203.14895

51. Kunc, K., Balkanski, M., Nusimovici, M.A.: Lattice dynamics of several a NB8-n compounds having the zincblende structure. II. Numerical calculations. Phys. Status Solidi (b) **72**(1), 229–248 (1975). https://doi.org/10.1002/pssb.2220720125

52. Tarasenko, A., Čtvrtlík, R., Kudělka, R.: Theoretical and experimental revision of surface acoustic waves on the (100) plane of silicon. Sci. Rep. **11**(1), 2845 (2021). https://doi.org/10.1038/s41598-021-82211-6

53. Zhuravlev, K.K., Goncharov, A.F., Tkachev, S.N., Dera, P., Prakapenka, V.B.: Vibrational, elastic, and structural properties of cubic silicon carbide under pressure up to 75 GPa: implication for a primary pressure scale. J. Appl. Phys. **113**(11), 113503 (2013). https://doi.org/10.1063/1.4795348